geosciences

MDPI

Article

Imaging Shallow Velocity Structure of an Inactive Fault by Airgun Seismic Source: A Case Study of Xiliushui Fault in Qiliang Mountain

Manzhong Qin [1], Baichen Wu [2,3,*], Yi Wang [2,3], Xueyi Shang [4], Yuansheng Zhang [1], Xuzhou Liu [1], Xiao Guo [1], Rui Zou [1], Yahong Wang [1] and Dianfeng Sun [1]

[1] Lanzhou Institute of Seismology, China Earthquake Administration, Lanzhou 730000, China; qinmzh@gsdzj.gov.cn (M.Q.); zhangys2011@gsdzj.gov.cn (Y.Z.); liuxz@gsdzj.gov.cn (X.L.); guox@gsdzj.gov.cn (X.G.); zourui@gsdzj.gov.cn (R.Z.); wangyh@gsdzj.gov.cn (Y.W.); sundf@gsdzj.gov.cn (D.S.)
[2] Institute of Earthquake Forecasting, China Earthquake Administration, Beijing 100036, China; wangyi@apm.ac.cn
[3] Innovation Academy for Precision Measurement Science and Technology, China Academy of Sciences, Wuhan 430071, China
[4] School of Resources and Safety Engineering, Chongqing University, Chongqing 400044, China; shangxueyi@cqu.edu.cn
* Correspondence: wubaichen990624@gmail.com; Tel.: +86-18810876260

Abstract: We observed high-quality waves from a repeatable airgun seismic source recorded by a linear ultra-dense seismic array across the Xiliushui fault zone, one of the inactive faults in the Qilian Mountain, on the northeastern margin of the Tibetan Plateau, China. We used Snell's law of seismic ray propagation to determine a simplified ambient velocity model. Based on the flexible and precise spectral element method, we computed broadband synthetic seismograms for a shallow low-velocity fault zone (FZ) to model the direct P-wave travel time delay and incident angle of the wavefield near the FZ. The FZ extent range and boundaries were inverted by apparent travel time delays and amplification patterns across the fault. According to prior information on the properties of the direct P-waves, we could constrain the inverse modeling and conduct a grid search for the fault parameters. The velocity reduction between the FZ and host rock, along with the dip angle of the FZ, were also constrained by the P-wave travel time delay systematic analysis and incoming angle of the P-waves. We found that the Xiliushui fault has a 70~80 m-wide low-velocity fault damage zone in which the P-wave velocity is reduced to ~40% with respect to the host rock. The fault damage zone dips ~35°southwest and extends to ~165 m in depth. The repeatability and environment protection characteristics of the airgun seismic survey and the economic benefits of a limited number of instruments setting are prominent.

Keywords: the fault zone seismic phase; airgun seismic source; fault zone imaging; body waves modeling; travel time inversion

Academic Editor: Hans-Balder Havenith

Received: 12 November 2024
Revised: 28 December 2024
Accepted: 2 January 2025
Published: 7 January 2025

Citation: Qin, M.; Wu, B.; Wang, Y.; Shang, X.; Zhang, Y.; Liu, X.; Guo, X.; Zou, R.; Wang, Y.; Sun, D. Imaging Shallow Velocity Structure of an Inactive Fault by Airgun Seismic Source: A Case Study of Xiliushui Fault in Qiliang Mountain. *Geosciences* **2025**, *15*, 16. https://doi.org/10.3390/geosciences15010016

1. Introduction

The study of the fine structure of faults, including the depth and formation of faults, has always been the core topic in exploration seismology, especially in areas where natural seismic data are lacking. While natural earthquakes can release substantial energy and produce formidable seismic waves, their occurrence is typically confined to specific locations and time frames, rendering them insufficient for the detailed exploration of local crustal structures due to their low resolution from the limited frequency content of the recording.

Natural earthquakes are often spatially and temporally localized and limited in number. In order to avoid the deficiencies associated with natural earthquakes, artificially controlled seismic surveys have emerged as a primary alternative, particularly in regions with low seismic activity. The utilization of advanced artificial seismic sources to generate active seismic waves has become a pivotal approach in shallow crust exploration, particularly for regional-scale imaging of structures and monitoring alterations in underground medium composition [1].

A chemical explosion is the most widely used onshore source among various artificial sources. The use of chemical explosions as a seismic source to study the elastic property of earth material can be traced back to the 1840s [2]. Seismic refraction and reflection experiments with explosive sources were carried out to image the crustal structure [3–5]. However, because of security and environmental issues, the use of chemical explosions has been more restricted in recent years.

In recent years, airgun seismic sources have been widely used in the detection of the crustal structure (upper crust, middle crust, lower crust, Moho, etc.) [6] and smaller-scale medium structure (faults, mineral resources, oil and gas resources, etc.) and the extraction of weak change information of underground medium, which has become an essential direction of seismological research [7]. A new type of airgun source has many advantages, such as the high repeatability of the trigger, high precision of locations, performance of control, high S/N ratio, and environment-friendly [8,9]. The airgun seismic source has the advantages of known source position, controllable excitation time, flexible and convenient distribution of observation system, dense observation, high repeatability, environmental protection, safety, and economy compared with explosive sources, noise sources, and repeated earthquake sources. The airgun seismic source has become an ideal source for underground medium monitoring because it can generate seismic waves by releasing high-pressure air in an instant underwater and causes only slight damage to the near field [10–13]. These conditions are helpful when calculating the travel time inversion. When using traditional methods to image a fault zone structure, the inherent problem of seismic source location error resulting from velocity model uncertainty exists in natural seismic source surveys, thereby increasing the imaging error for exploring the fault zone properties.

Many researchers have used various methods based on natural earthquakes to study the whole large structure information of fault zones, such as the method of body wave arrival delay of local and teleseismic events [14,15], analysis of body wave amplification pattern of local events [16,17], and the inversion of the fault zone trapped waves (FZTWs) [18,19]. Although the above methods can be used to analyze the low-velocity characteristics of FZs quantitatively, many questions about the structural characteristics of the low-velocity zone of FZs remain unclear, such as the dip of the low-velocity zone (LVZ), the depth range, and the accurate value of the velocity reduction relative to the host rock. In addition to the qualitative analysis of fault zone location based on the seismic observation records described above, seismic imaging and inversion techniques have been advancing to explore the critical information of FZs.

It is still difficult to accurately constrain the key parameters of fault zone LVZs, such as the depth range, which still have obvious compromises for seismic inversion with a finite seismic phase. For example, in the study of the high-resolution structure of the Chenghai Fault (CHF) in Yunnan, China, the LVZ depth of ambient noise tomography inversion is overestimated, which is reflected in the overestimation of the arrival of teleseismic S-waves recorded by the same array [15]. In addition, Jiang [20] also obtained the P-wave velocity structure and shallow LVZ depth below the same array using the teleseismic receiver function. Based on the receiver function inversion, the resulting Vp and Vs models can better match the delay time of the observed array recording of the teleseismic P- and

S-waves. Due to the reasonable simplification of the efficient inversion of the complex shallow LVZ receiver function, the model with multilayer and transversal variables must be simplified to a single-layer model in half space.

Firstly, to constrain the structure of the FZ, we need to deploy ultra-dense long-aperture arrays along a typical FZ to improve the LVZ imaging resolution. Based on the long ultra-dense array, more correlated seismic phases near the FZ can be identified, and the model can be used to invert a more detailed and comprehensive FZ structure. The development of the dense arrays will not only provide higher-quality data but it will also facilitate the development of new seismic imaging techniques (such as multi-phase joint imaging of fault zones using more waveform records).

Secondly, the problem of data scarcity can also be solved by using artificial sources to investigate the fault where seismic activity is rare. The artificial source can be actively controlled in space and time according to the research requirements and can be excited at high frequencies to produce clear reflection and refraction phases. High-quality artificial sources (such as high-volume airgun excitation, methane, etc.) provide a powerful tool for monitoring spatial and temporal changes in the physical properties of FZs, which can advance our evolving understanding of FZs.

In the future, using full-waveform inversion techniques with multiple seismic phases may provide a more accurate structure characterization of FZs. Overall, it is a challenge to continually improve and integrate various seismic techniques to improve our understanding of FZs' structure and associated seismic behavior. And in the future, we can use the above method to study faults on a large scale and efficiently determine the structural characteristics of faults within the range of active source detection.

2. Tectonic Setting and Data

Linear Ultra-Dense Array Deployment and Airgun Seismic Source Data Acquisition

The Gansu Qilian Mountain active source is located on the northeastern margin of the Tibetan Plateau, China (Figure 1). It is one of the three airgun seismic source signal launching centers built in mainland China with large-capacity airguns, which are called Fixed Airgun Signal Transmission Stations (FASTSs), in Yunnan, Xinjiang, and Gansu. Since 9 July 2015, the Qilian Mountain active source has been officially in use for excitation operations; the maximum water depth of the excitation point is 65 m, and the maximum detection distance of the P-wave is ~400 km [21–23]. The maximum detection distance is affected by the complex local crustal structure and the relatively dense population will generate a relatively high level of noise to reduce the detectable distance [24].

The active source monitoring area is mainly located in the compression suture zone between the Qaidam block and the Alxa block (Figure A1a). The main faults include the Qilian Mountain northern margin fault zone, the Changma-Ebo fault zone, the Yumushan fault zone, and the Longshoushan fault zone [25–27]. In this study, an inactive old fault was detected by the airgun seismic source excited by the active source of the Qilian Mountain in Gansu province, China. Through repeatable airgun excitations, the fault zone within the monitoring range (which can reach up to 300 km) can be conveniently surveyed. The waveform data recorded by seismometers can be stacked to improve the SNR. After that, we will determine the width, depth and dip of the Xiliushui fault zone by analyzing the direct P-wave travel time characteristics and the incoming angle observed in the stations across the fault.

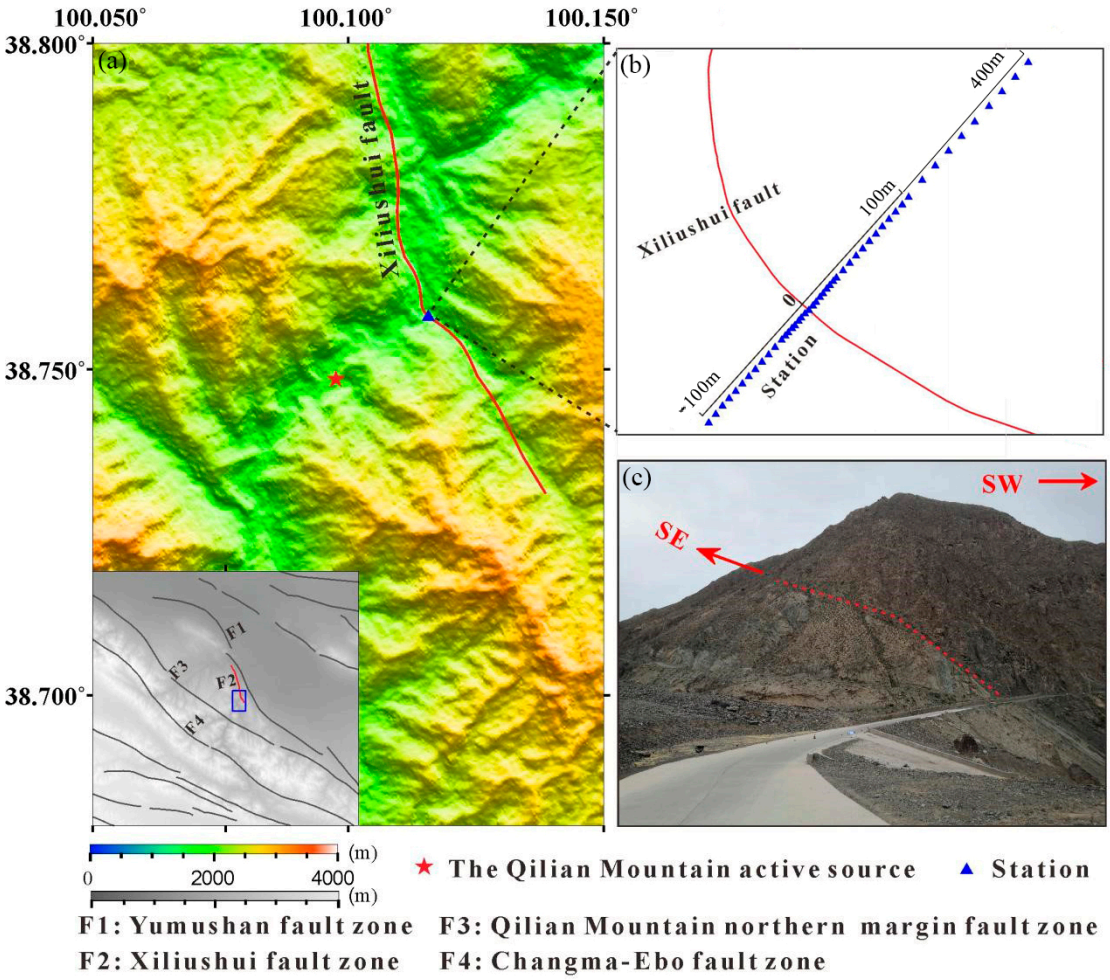

Figure 1. The location of the Gansu Qilian Mountain active seismic source and Xiliushui fault zone. (**a**) In the monitoring area (blue box), the red star represents the location of the airgun and reservoir. In the topographic map of the window, red line represents Xiliushui fault. (**b**) A linear dense array with a length of 500 m across the Xiliushui fault; the fault (red line) is outcropped on the surface. (**c**) The strike and the dip of the fault are SE and SW from surface geology survey, respectively. The aerial view of reservoir and station location in the study area is shown in Figure A1.

We investigated several fault zones in the Gansu Qilian Mountain active source monitoring area. The Xiliushui fault, about 1.8 km away from the excitation center, which is an inactive fault, was selected as the detection object, according to the field experiment conditions. The fault is outcropped on the surface (Figure 1c) and developed in Ordovician tuff; the strike and the dip of the fault are SE and SW, respectively (Figure 1b). Meanwhile, the fault is close enough to the active source airgun we set up to make it convenient to observe the signal with the fault feature [28], and inactive faults are not time-varying, allowing us to conduct various long-term seismic surveys with limited instruments. Because of the waveform stability of the airgun source, researchers can use the 'rolling deployment' method to deploy the station, so as to save observation costs.

In May 2019, we conducted an experimental observation of a linear ultra-dense array across the Xiliushui fault with an aperture of 500 m. The array, equipped with electronic portable seismometers (EPSs), was centered at Station_0 (0 m) with stations spaced at 1.0 m near the surface fault zone (FZ) and 2.0 m elsewhere. The sampling rate was set at 500 Hz.

We used one airgun from the Gansu Qilian Mountain active source for the excitation experiment, maintaining a consistent working pressure of 2000 psi (calculated according to Ronen [29]), which is equivalent to about 2 kg of explosives. Due to the short distance

(about 1.8 km) between the excitation source and the linear seismic array, each excitation took 2–3 min. Based on the waveform stability of the airgun source, we used 16 stations in a "rolling deployment" along the array. To ensure reliable observation of the waveforms, we conducted the excitation approximately 10 times. Using this method, costs can be saved. We examined the waveform uniformity of each excitation (Figure 2), and the observed waveforms show that the "rolling deployment" method is feasible. According to similar research, waveform data generated by recently developed large-volume airgun arrays can be used for geophysical surveys [30]. This novel and environmentally friendly artificial seismic source is termed a transmitting seismic station (TSS), which has a large excitation capacity and is easy to control. The entire "rolling deployment" can be completed very efficiently within half a day, which can be applied to other seismic surveys by a TSS.

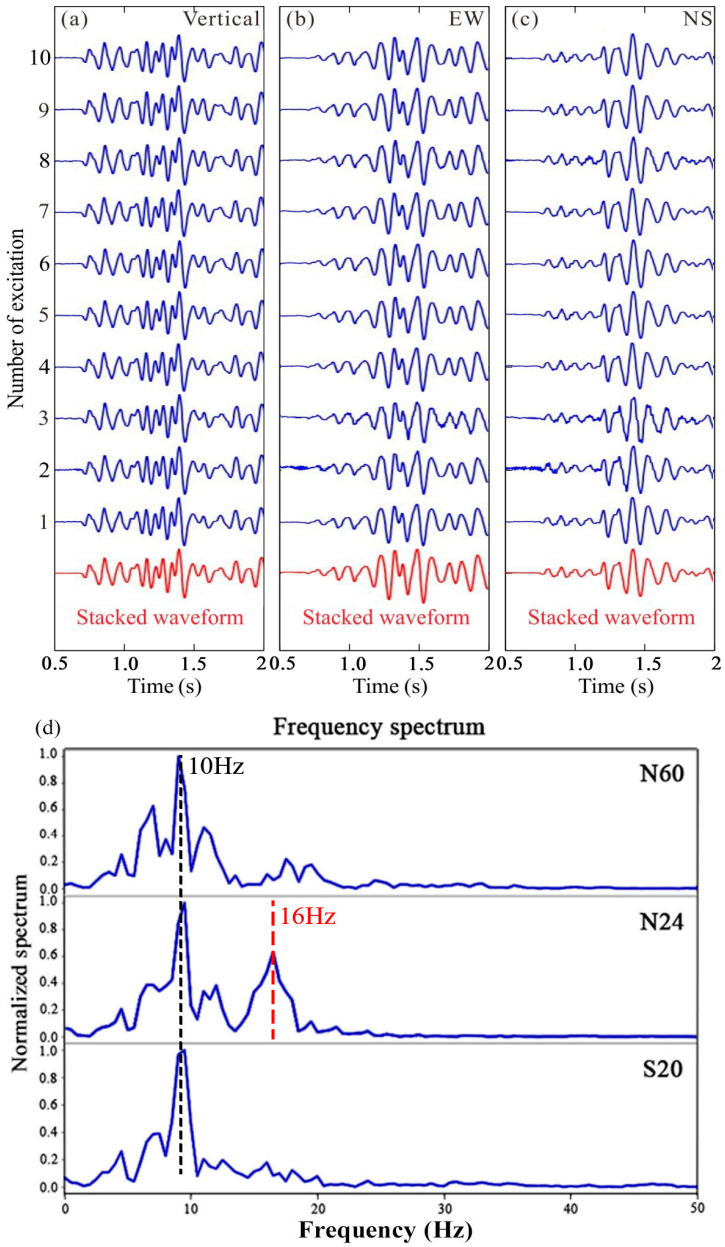

Figure 2. (**a**–**c**) The three-component observation waveforms (blue) of airgun seismic source excitation recorded at Station_N24 (24 m); the red traces are the stacked waveforms. (**d**) The frequency spectrum of station near the FZ recorded at Station_S20 (−20 m), N24 (24 m), and N60 (60 m).

In this section, we introduce the geological structure background of the fault and the feasibility advantages of the airgun source compared with other natural earthquake sources. Finally, we describe the process of collecting the seismic data. In the next section, we describe the detail of the waveform data used in this study and identify the types of P-wave, surface wave and S-wave. Section 3 presents the results based on the peak ground velocity analysis and standard spectral ratio analysis at stations across the array and calculates the delay time curve of the P-wave and surface wave. Combined with the arrival time inversion in Section 4, the results indicate the structure and physical property parameter of the FZ.

3. Data Processing

The Reservoir_Station mainly observed the airgun seismic source signals on the reservoir's shore. We used the Reservoir_Station observation data to extract the excitation time of the airgun seismic source and cut the excitation waveforms from all the observation stations on both sides of the fault according to the excitation time. As the excitation energy of a single airgun is strong enough and relatively close between the excitation position and the linear dense array, the excitation waveforms can be observed at stations on the linear array. Each station's corresponding observation waveform across the fault is obtained by stacking the multiple excitation waveforms on three components (Figure 2). We selected the stacked waveform data inside and on both sides of the fault and calculated its spectrum. Due to the frequency of the waveforms being mainly concentrated between 5 and 20 Hz (Figure 2b), we applied a band-pass filter (5–20 Hz) for the stacked waveforms recorded by each station to remove noise. In Figure 2, unlike the other stations in the fault zone, we find the frequency spectrum of Station_N24 has two peaks, 10 Hz and 16 Hz. We infer that the peak frequency of 16 Hz is caused by the fault structure. In order to study the dominant frequency response characteristics of the 10 Hz airgun source signal, we further applied a band-pass filter (5–12 Hz) to research the S-wave and surface wave in a time window of 1.1–1.5 s (Figure 3).

As expected, clear P-body wave phases were observed in seismograms for the explosion and airgun [24]. In our study, the P-body waves were clearly observed in the ZR component observation waveforms (Figure 3a). However, in a controlled explosion source experiment, surface waves (Lg) usually overlap S-waves [31]. Note that the airgun seismic source is different from natural earthquakes, since the airgun in the water triggers the seismic event. Since S-waves cannot be generated in the water, the overall excitation of S-body waves cannot be substantial, and most of them are converted from P-waves in the velocity interface along the wavefield propagation path. In Figure A2, we used SPECFEM2D (Version 8.1) to model the airgun wavefield in a local velocity model with topography. The airgun source is triggered in water and we find stable surface waves generated by topography and path-converted waves in the target area. In Figure A2, we can observe that the S-wave is affected by the complex terrain to generate scattered waves and reflected waves in the propagation path.

In order to identify surface waves (Lg) and S-body waves, it is necessary to examine the trajectory of particle motion using three-component recordings to judge Rayleigh waves. Due to the horizontal component of the surface wave having stronger energy than the vertical component, we used 1.1–1.5 s as the surface wave arrival time window based on the horizontal waveforms. Nine stations were selected along the array at equal intervals to observe the changes in the particle trajectory (Figure 3). Then, we used this time window (the color band region in Figure 3a) to plot the particle motion using the vertical (Z) and radial (R) components of the waveform (Figure 3b). If the trajectory of the particle motion is a retrograde ellipse in the corresponding time window (Figure 3b), that represents a

Rayleigh-type surface wave; we then checked the Rayleigh-wave group velocity dispersion curve from the R-component (Figure 4). We used the method of frequency–time analysis based on Hilbert transform to extract the travel time delay of the waveform packet at different frequencies.

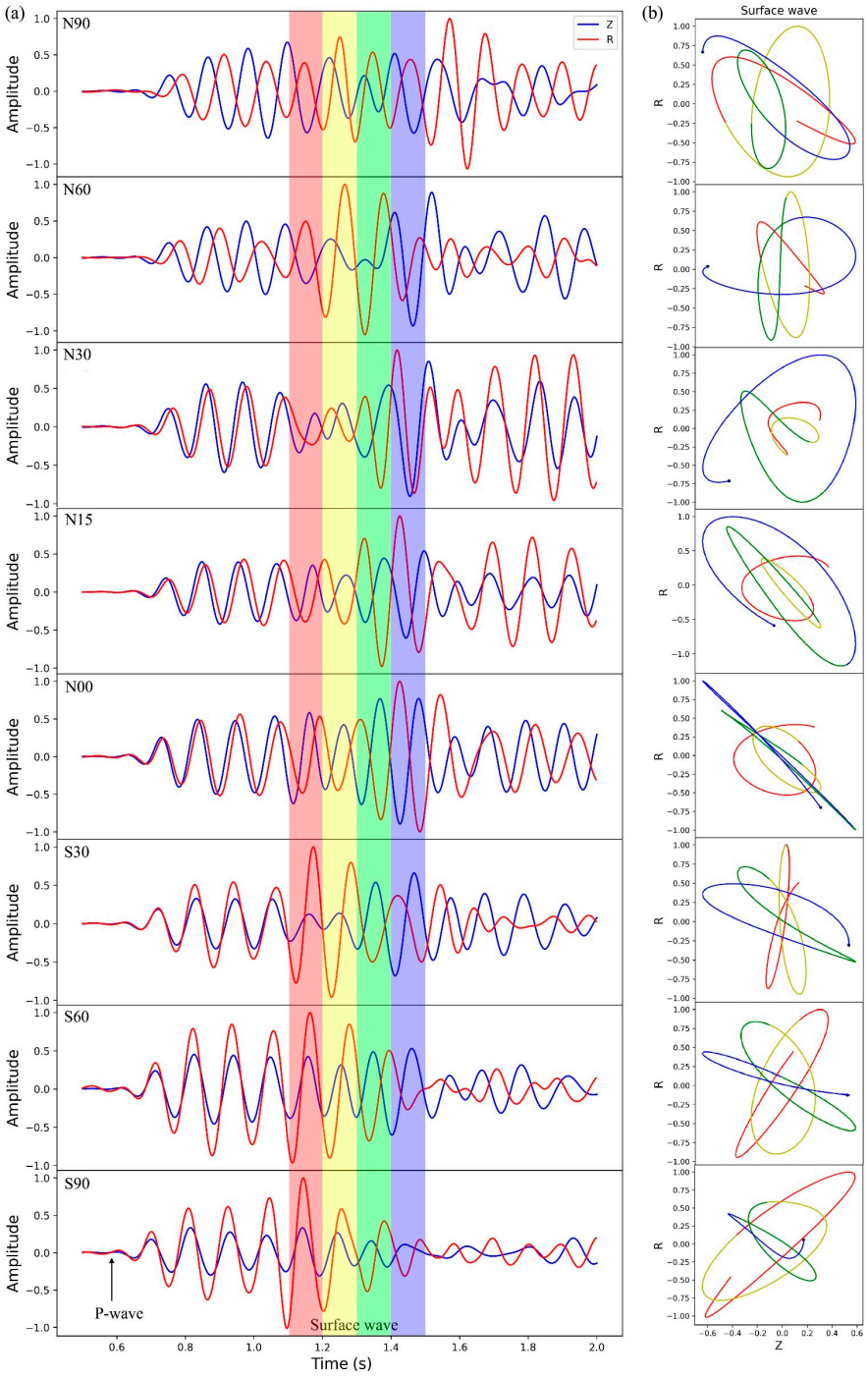

Figure 3. (**a**) The Z-component (blue line) and R-component (red line) observation waveforms in the bandpass 8–12 Hz of airgun seismic source excitation recorded at Station_S90 (−90 m), S60 (−60 m), S30 (−30 m), N00 (fault trace), N15 (15 m), N30 (30 m), N60 (60 m), N90 (90 m). (**b**) Particle motion of the waveform in the different color-shaded window in (**a**). The big point represents the end point of the particle motion.

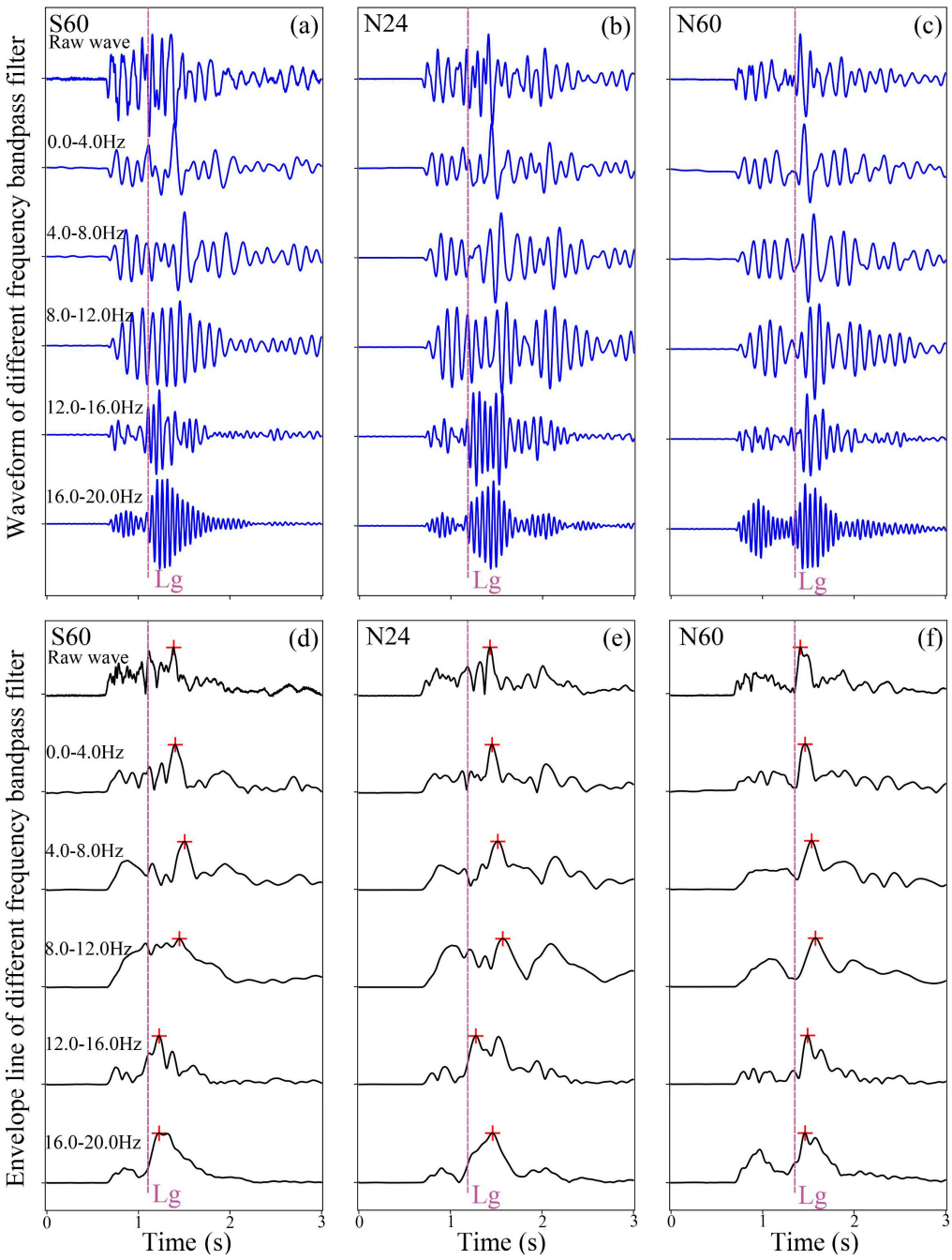

Figure 4. The multi-band (0–20 Hz) filtering (**a**–**c**) and corresponding amplitude envelope (**d**–**f**) of observation waveforms at representative station_S60, N24 and N60, where the raw wave represents observation stacked waveform from R-component, and the red dotted line indicates the arrival time of surface wave.

In order to study the dispersion characteristics of the surface wave, we chose the recording waveforms of Station_S60, N24 and N60 with the larger amplitude spectrum peak values filtered in bandpass 0–20 Hz (Figure 4a–c). Figure 4d–f show the corresponding amplitude envelopes obtained by the Hilbert transform method. The peak value of the envelope indicates the wave energy's arrival in the corresponding frequency band. The results show that the complex frequency dispersion phenomenon exists in the surface wave section, and its propagation velocity is related to the frequency and complicated subsurface velocity.

The P-waves and surface waves are observed in the Z- and R-component observation waveforms (Figure 5). In addition, the waveforms with fault zone characteristics are also observed, which appear about 0.2 s after the surface wave. Compared with the P-body wave, the surface waves in the fault zone have the characteristics of longer durations and higher amplitude, and the stations close to the fault zone are more obvious (Figure 5, the red dashed rectangle). The low-velocity characteristics of body waves in fault zones have been confirmed by observing some faults. For example, body and code waves with longer periods and larger amplitudes can be generated [14,15]. Many researchers have used the fault zone trapped waves (FZTWs) generated from natural earthquakes to inverse the physical properties of FZs [32]. Compared with natural earthquakes, we found that the airgun sources generated more surface wave components and were confused with S-waves, which made it difficult to use the FZTW pattern to match and invert the physical parameters of the fault. In this paper, we use the clearer P-wave to invert the structural and physical parameters of the fault.

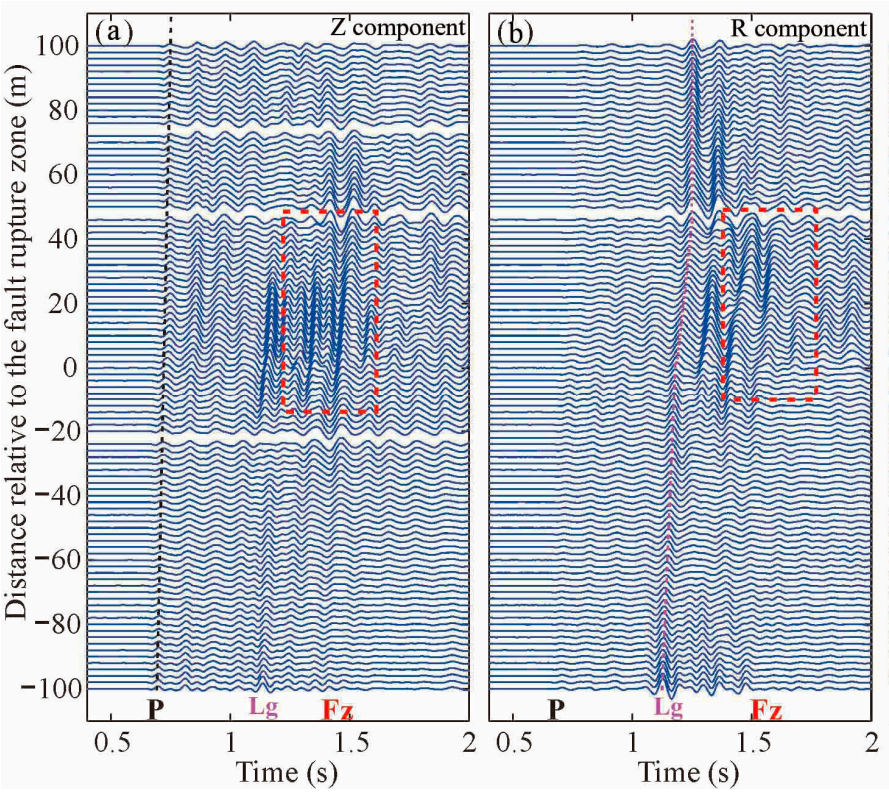

Figure 5. The filter-stacked (**a**,**b**) observation waveforms in the Z- and R-component stations across the fault. The dotted line represents the arrival time of P-body wave (black dotted line) and surface wave (purple dotted line), and red dotted rectangle boxes represent the fault zone waveform observed by three-components stations close to the fault zone.

3.1. Peak Ground Velocity

The peak ground velocity (PGV), defined as the largest amplitude in the velocity seismogram, has been shown to correlate well with the seismic intensity and earthquake damage to surface structures [32]. The small-scale spatial changes in PGV values are often attributed to the heterogeneity near the surface and, in return, can be used to infer the lateral variation of subsurface structures [33].

We observed some code waves that characterize the fault, especially as shown in the red dashed rectangle in Figure 5. In this section, we use the observed enveloping of the ground velocity waveforms from the fault-parallel components recorded by each station

to examine the PGV, RMS, and its spatial variability across the array. The waveforms are bandpass filtered between 5 and 20 Hz, as seismic energies of recorded waveforms broadly fall into this frequency range. Following Qiu et al. [14], the PGV and RMS values within the surface wave time windows were respectively calculated for each waveform. The PGVs and RMSs for the horizonal components showed a peak trend within the fault zone; their results are included in Figure 5.

Figure 6a was generated by stacked waveforms, corrected for the instrument response, rotated clockwise to the fault-parallel component (45°), and integrated into displacement. The green band shown in Figure 6b marks the high-value area of the black curve, with a width of ~75 m. To demonstrate the motion amplification effect after the surface wave at the entire array, we used the peak ground velocity (PGV), duration of high amplitudes, and root mean squares (RMS) of the surface wave to identify the stations with FZTWs. Figure 6b shows the distributions of the PGV and RMS of the fault-parallel component surface wave, normalized by the maximum value of the entire array. Stations with FZTWs are characterized by large values of PGV and multiple RMS, indicating considerably higher amplitudes than the rest of the array (as depicted in Figure 6b, black curve).

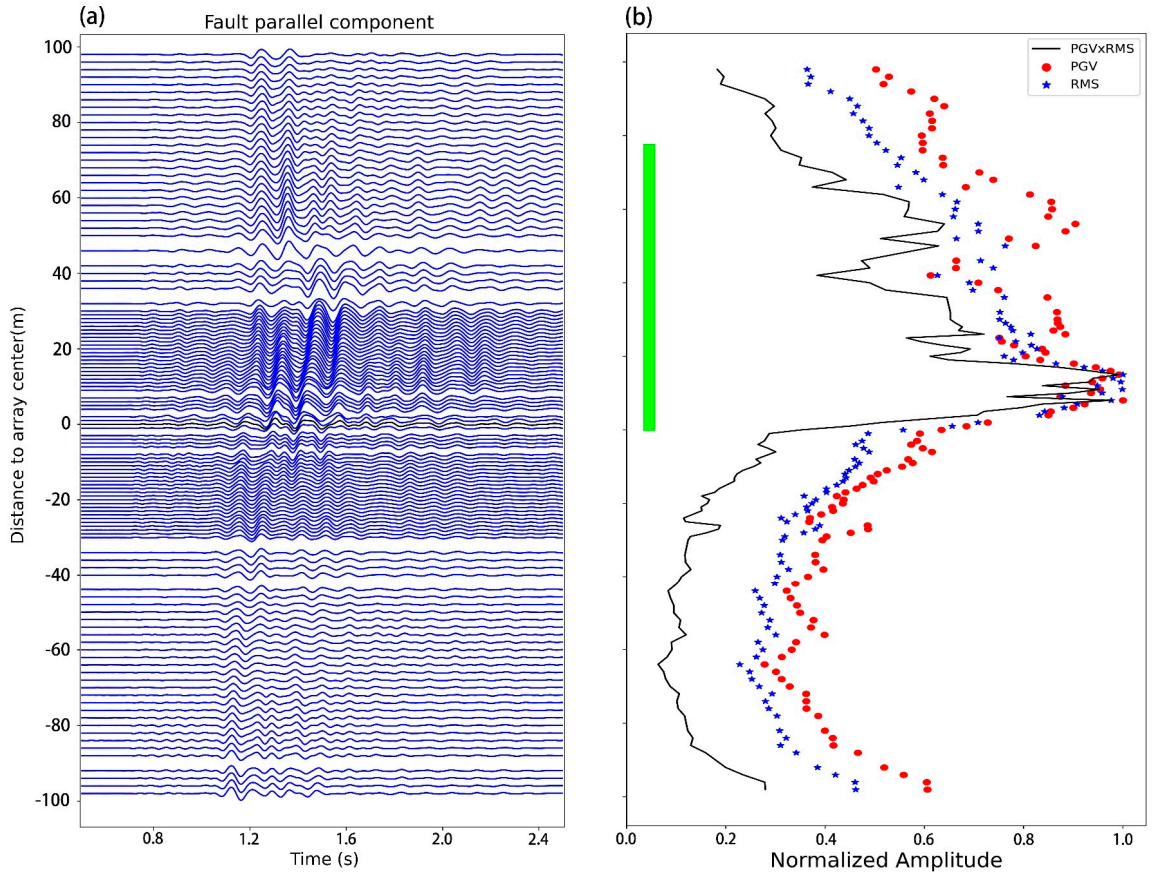

Figure 6. (**a**) Fault zone trapped waves (FZTWs) following surface wave arrivals (along the line of the array) after being rotated clockwise to the fault-parallel component (45°). (**b**) Distributions of normalized peak ground velocities (PGVs; red dots) and root mean square (RMS) amplitudes (blue stars) of the surface waveforms shown in (**a**). The black curve represents the likelihood of FZTWs (i.e., the normalized multiplication of PGV and RMS values) and is used to identify FZTWs. The green bar outlines the stations with FZTWs.

3.2. Standard Spectral Ratio

The standard spectral ratio (SSR) [34] method is the most commonly used method for studying low-velocity effects. The SSR method is computed as the ratio of the Fourier

spectra of the earthquake ground motions between the target station and the reference bedrock-site station, which is considered as an amplification "free" site [35]. In order to further analyze the characteristics of the low-velocity zone, here we apply the standard spectral ratio method to the observed horizontal ground motions. Only the recordings of horizontal components were used because horizontal ground motions are more sensitive to variations in horizontal velocity and are affected by the site conditions to a much larger extent than vertical ground motions [36]. This study analyzes the horizontal component recording to validate the FZ derived from Figure 6.

The SSR method requires a reference station, usually on the bedrock, where the observed ground motions could be considered input for other nearby sites [33]. We chose five stations (Station_S60–Station_S70) at the SW side of the array as reference stations to eliminate the instability of a single reference site, as with the PGV analysis. The waveforms and spectra at the reference stations were inspected and found to be similar and have clear wave signals without a code wave. We calculated all the initial Fourier spectra after cutting the wave amplitude spectra from 5 to 20 Hz within 0–2 s time windows. We calculated a reference horizontal spectrum ($U_{(i,ref)}(f)$) by taking the average of the horizontal spectra at the five reference stations:

$$U_{ref}(f) = \frac{1}{5}\sum_{k=1}^{5}\sqrt{R_k}\sqrt{T_k} \quad (1)$$

Then, the spectral ratios across the array were calculated by using the spectrum of the array site divided by the reference horizontal spectrum:

$$SR_i(f) = \frac{U_i(f)}{U_{ref}(f)} \quad (2)$$

where U_i (f) is the horizontal spectrum at station i. Several station seismic records with low quality were removed to ensure reliability.

High spectral ratios between 16 and 17 Hz were observed in the middle part of the array, and much stronger amplification effects appear within the identified low-velocity zone and core damage zone. In Figure 7, we mark the location of the fault according to the high spectral ratio zone. Around the rupture trace (zero-offset), a ~75 m-wide zone is characterized by the highest amplification factors in the spectral ratio map at ~17 Hz.

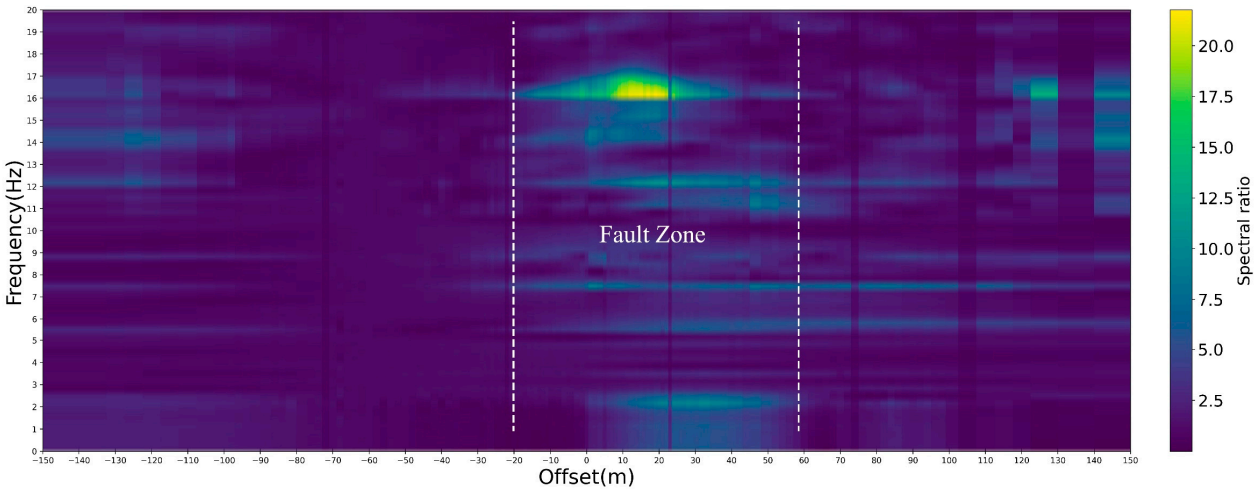

Figure 7. The spectral ratio results along the entire array obtained from horizontal component. The white dashed zone indicates high spectral ratio value.

3.3. Body Wave Arrival Time Delay Analysis

We manually picked P-body wave and surface wave arrivals from raw waveforms using the ObsPy (version 1.0, based on python) software and then double-checked the first phases on the filtered data (5–20 Hz). In total, all the stations' P-body wave and surface wave phases were picked in the dense array, respectively. As shown in Figure 8, we calculated all the P- and surface wave phase arrival times through the cross-correlation method. Among them, the difference in P-wave arrival time between the southwest terminal station and the northeast terminal station was about 60 sampling points, and the difference in surface wave arrival time was about 100 sampling points. Low-velocity anomalies existed at positions 0–75 m and near 250 m (imaging not used). This research focuses on the fault region near 0–75 m. We used this method to calculate the regional wave velocity (apparent velocity) as a reference (Vp = 4.67 km/s, Vlg = 2.8 km/s), which was used for setting the max velocity model parameters in the travel time inversion section. According to Snell's law (Equation (1)), the velocity values above can only represent the velocity at the bottom of the model.

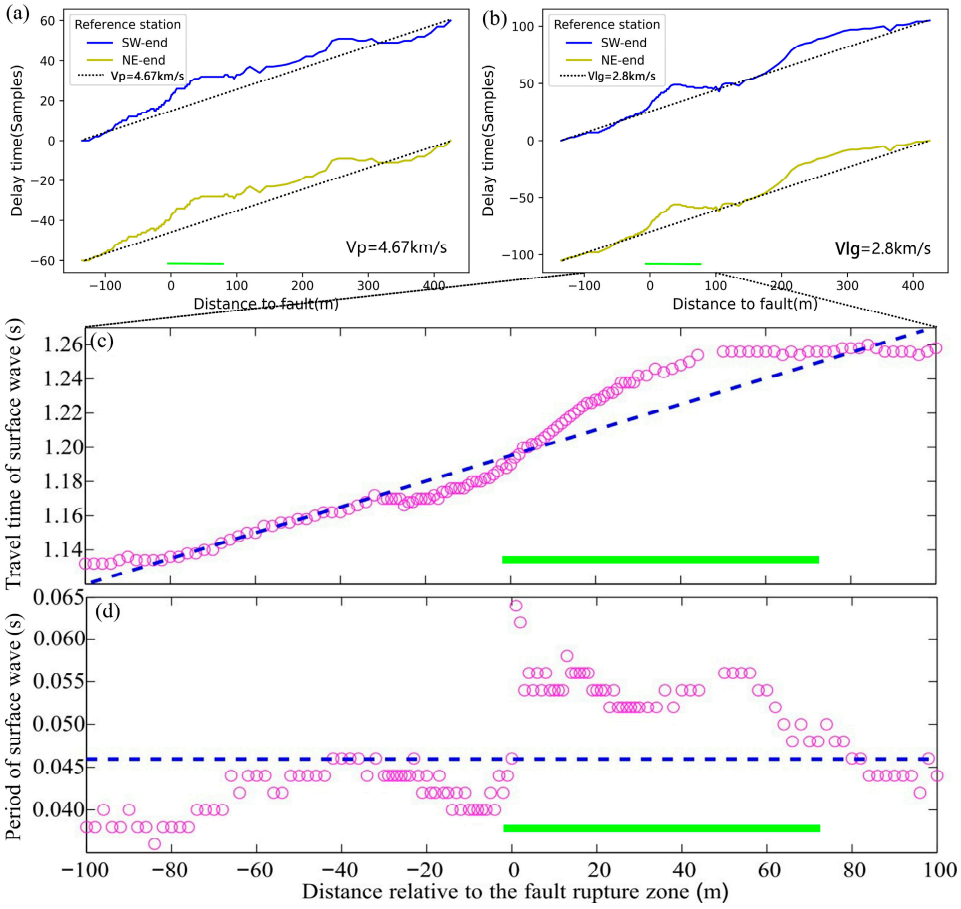

Figure 8. The cross-correlation method calculates the P-wave and surface wave, generated in R-component by airgun excitation. (**a**) represents the P-wave arrival time and (**b**) represents the surface wave arrival time. The yellow and blue curves represent the results obtained using different reference stations. Dotted line represents fitting regional velocity. P-wave velocity is 4.67 km/s and surface wave is 2.8 km/s as the regional maximal seismic wave velocity, which is the model velocity at the bottom. The green bar outlines the stations in fault zone. Arrival time (**c**) and period characteristics (**d**) of surface wave in R-component (Figure 5b) of all stations across the fault zone. The green bar outlines the stations in fault zone.

The frequency of the waveforms is calculated in the low-velocity fault zone (Figure 4). We measured the arrival time and period of the surface wave in the R-component of all the stations across the Xiliushui fault zone (Figure 8). The travel time delay of the surface wave recorded at the stations near the fault zone was significantly larger than that far away from the fault zone stations. The travel time delay was about 0.02 s (Figure 8c), related to the surface wave propagating through the low-velocity fault zone.

4. P-Body Travel Time Inversion

In previous studies, FZ imaging and multi-seismic phase analysis are usually based on the asymptotic ray hypothesis. For example, in the travel time tomography of typical seismic phases, the structure characteristics are estimated by minimizing the misfit function between the observed travel time of the seismic phase and the calculated travel time of the ray [37]. Under the ray theory, the seismic data are infinitely high frequency, and the wave propagation is only affected by the structure in the ray path, not by the structure outside the infinitely narrow ray path. In fact, this is contrary to the finite bandwidth characteristics of the actual seismic propagation [38]. For the present body wave travel time tomography in the FZ, only the travel time of the initial arrival phase or the main phase with the highest signal–noise ratio (such as direct P- and S-waves) is usually used, and the amplitude and seismic phase of the waveform recording with rich information is not used. This method results in low resolution of the imaging results of the target structure [39].

Waveform inversion techniques theoretically proposed in the 1980s use more characteristic information in seismic recordings than ray-based travel time tomography [40]. By minimizing the misfit function between the observation and synthesis of the seismic waveforms, waveform inversion can accurately estimate the multi-scale structural features in the crust model (from rough large-scale varying structures to small-scale fine features). It can accurately invert both the coarse and fine features of the target model. The multi-scale resolution of waveform inversion is achieved by designing appropriate misfit function and fully exploring waveform information in different frequency bands. Despite inherent challenges such as offset limitations and complex near-surface structures, the applicability of waveform inversion to real land data has also improved in recent years [41,42].

Waveform inversion of actual marine data has achieved remarkable success and has become one of the main means of exploration of offshore oil and gas resources. In recent years, the applicability of land seismic data for high-resolution waveform inversion has also improved; for example, large-offset seismic phase waveforms recorded by deep reflection in southern Tibet were used to image crustal structure details [43] and time–frequency waveform inversion to reconstruct shallow structures [44]. Although waveform inversion can provide high-resolution model parameters, there are some obstacles to applying it successfully, including the strong nonlinear relationship between the wavefield and model parameters, the non-convexity of the misfit function, the complexity of the propagation medium, and the high computational cost of solving the wave equation. Therefore, some researchers have proposed some improved waveform inversion strategies that are more suitable for field applications, such as early arrival waveform inversion [45], adaptive waveform inversion [46], and the envelope waveform inversion method [47].

For the data in this paper, because they were created by a single position-controlled source excitation, they lack the data cross-coverage required for tomography or waveform inversion. Considering the unidirectional propagation characteristics of the actual data and the detection target, we used wave equation modeling to fit the most reliable waveform information: the wide-band cross-correlation travel time of the initial P-wave [48]. Although it is not possible to calculate the standard inversion process, we can use the grid search

method to sufficiently constrain the key structural parameters of the target FZ through the wave equation modeling and matching the data records by modeling the waveform.

4.1. SPECFEM2D for Wave Propagation Modeling

Different numerical methods, such as the finite difference method (FDM) [49], finite element method (FEM) [50], pseudo-spectral method (PSM) [51], and spectral element method (SEM) [52,53], can be used to solve wavefield equations. SEM is halfway between the FEM and PSM methods. It can incorporate the flexible geometry of FEM and subdivide the computational domain into non-overlapping elements. SPECFEM2D, based on SEM, is a powerful software package for modeling seismic wave propagation at local or regional scales. The method combines the flexibility of the FEM method with the accuracy of the SEM method, which will significantly simplify its algorithm and reduce computing time [54].

4.2. Seismic Source Parameters and Regional Fault Model

We started the process by constructing a regional mesh using the built-in meshing tool of the SPECFM2D_cartesain package to build the regional mesh with a ~1 km depth. The airgun seismic source and excitation process used in this experiment are different from the natural earthquake source. In seismic forward modeling, the Ricker wavelet source is often used as a seismic source, which has been shown to be a very efficient means of describing the signal's spectrum [55]. In this paper, the single Ricker wavelet source time function with a dominant frequency of 10 Hz was used:

$$f(t) = \left(1 - 2\pi^2 f^2 t^2\right) e^{-\pi^2 f^2 t^2} \tag{3}$$

where f is the frequency of the source, which is set as 10 Hz.

The highly accurate spectral element method [56] was employed to solve the forward modeling. Considering the complexity of the strata, the simple "sandwich" fault structure may not be able to achieve the ideal inversion effect, so we needed to create topography data on this basis and used the SPECFEM2D to simulate the whole experiment process.

The P-wave travel time curve of the synthetics and observation filtered at 10 Hz were used to construct the normalized cross-correlation coefficient (NCC) as the travel time misfit function:

$$r\left(T_{obs}, T_{syn}\right) = \frac{Cov\left(T_{obs}, T_{syn}\right)}{\sqrt{Var[T_{obs}]Var\left[T_{syn}\right]}} \tag{4}$$

where T_{obs} represents the observed travel time of the source–receiver combination; T_{syn} represents the predicted travel time based on the current fault model; Cov (T_{obs},T_{syn}) is the covariance between T_{obs} and T_{syn}; and $Var[T_{obs}]$ is the variance in T_{obs}. According to the above misfit function, we can better quantify the quality of the fault model based on the P-waves.

The parameters and material velocity of the fault, strata, and water reservoir are listed in Table 1. It should be noted that the P velocity model of the fault zone and host strata is calculated based on Snell's law [57]. Considering the horizontal layered strata and the regional velocity model satisfies a linear velocity gradient, the P-wave velocity is directly proportional to the depth. Due to the limited observational data, according to the P-wave regional apparent velocity (Figure 8a) and the angle of the P-wave incidence, the P-wave surface slowness (u_0) and the surface incident/incoming angle (i_0), the following formula is used:

$$u_0 \sin i_0 = p = u \sin i \quad (5)$$

where u is the ray slowness and i is the ray incident angle. Before the P-wave incident fault, the P-wave incoming angle is about 50°;we infer that the P-wave velocity is 3.58 km/s. According to previous research [58], the wave velocities (Cp and Cs) filled with water are chosen as 1500 and 0 m/s, respectively.

Table 1. Parameter setup of the SPECFEM2D velocity models.

Parameter	Lower Boundary	Upper Boundary	Increment
FZ velocity reduction ratio	35%	65%	5%
FZ horizontal shift	0 m	40 m	5 m
FZ dip angle	0°	60°	5°
FZ width	50 m	90 m	10 m
FZ depth	125 m	325 m	10 m
Host strata velocity	3.58 (km s^{-1})	4.67 (km s^{-1})	Linear
Water reservoir velocity	1.5 (km s^{-1})	1.5 (km s^{-1})	Fixed

Many parameters can be roughly constrained by prior information from the properties of the CCTT curves of direct P waves, such as the width of the FZ and the FZ central location. Other parameters, which are difficult to estimate, can be initially estimated with a coarse grid search first. These prior constraints and preliminary coarse searches are aimed at reducing the number of forward numerical modeling required for the grid search. Finally, the search ranges and increments of the fine grid search for FZ parameter are described in Table 1. We used the grid search strategy to compute approximately 80,000 models, and selected the model that best fit the detrending cross-correlation travel time of direct P data as the inversion solution.

4.3. Seismic Modeling Workflow

Seismic forward modeling techniques, encompassing ray trace modeling (referenced in works by Withjack and Pollock [59]; Fagin [60]) and wave equation modeling [61–63], have been employed to investigate the seismic characteristics of various fault zones and other geological structures.

In this study, 2D wave equation seismic forward modeling was conducted. The complete workflow of the seismic forward model used in this study involved three major steps (Figure 9): wave equation forward modeling, travel time curve NCC value calculation, and model analysis. After generating thousands of different velocity models, we picked the velocity model with the highest travel time curve NCC value.

We constructed an in-depth velocity model using a polygon-based representation in our forward modeling approach. Each velocity variation was constrained within a defined polygon. A fundamental velocity polygon comprises P-wave velocity. Once the velocity models in depth were established and the acquisition parameters were configured, we proceeded with the P-wave forward modeling. The resulting shot gathers were then utilized for the subsequent processing steps.

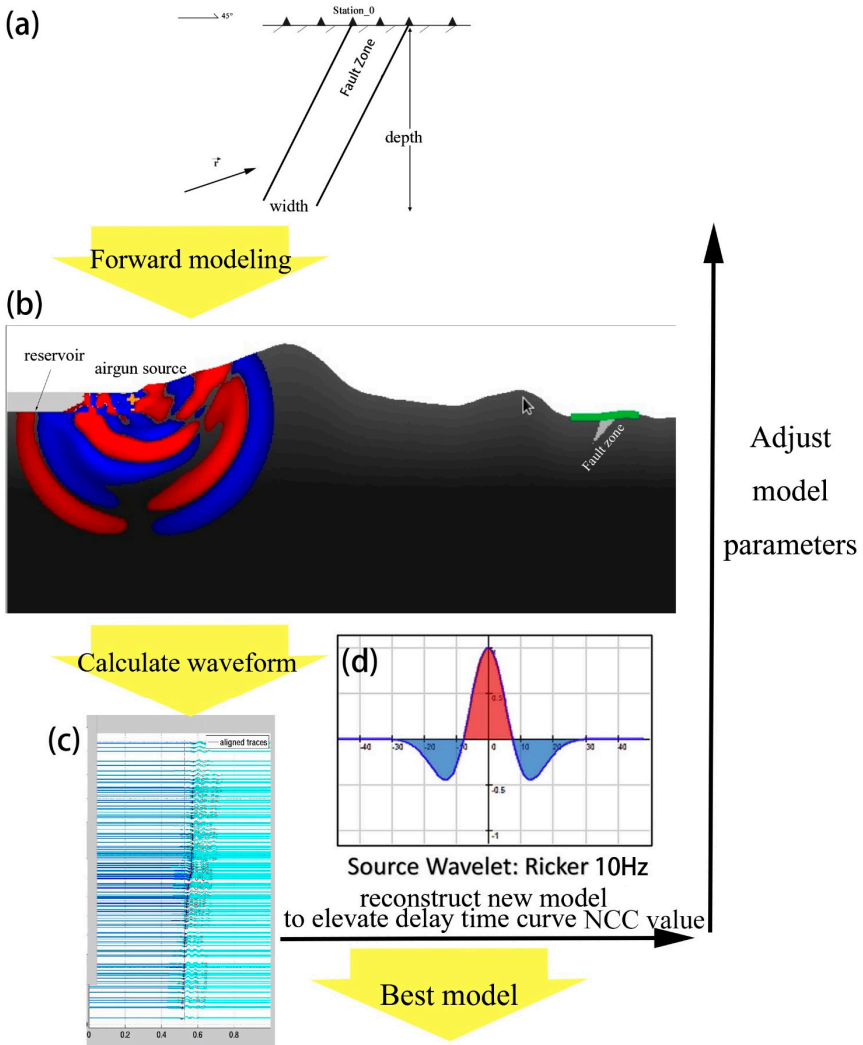

Figure 9. A workflow showing the key steps in the seismic forward modeling method used in the study: forward modeling, CC value calculation, and velocity analysis. (**a**) Fault model in depth and width. (**b**) Snapshot of the wave propagation and the shot gathered from the same source. (**c**) Synthetic waveform figure. (**d**) The waveform of the source wavelet: Ricker with a frequency of 10 Hz.

4.4. FZ Location and Dip Extents

Seismic modeling of the variously inclined faults was conducted using a series of controlled experiments. We first constructed models that explored the effects of the P-wave travel time difference within the fault by considering two possibilities: the location and dip of the fault. Based on the above research and field observations, we gained a basic understanding of the shape of the fault. In previous field observations of the Xiliushui faults, we measured the dip of the fault based on its surface trace. However, we could use a different method to constrain the dip of the fault underground. Therefore, we tried to constrain the precise shape of the fault by combining its position and dip. By fine-tuning the position of the fault core and fault dip in the model and comparing the misfit value between the theoretical travel time curve and the observed travel time curve, we could determine the optimal shape of the fault (Figure 10). Figure 10 shows the misfit matrix based on the cross-correlation P-wave travel time, when the P arrival times for different FZs dip angle from 5° to 50° and the fault zone core location from 5 m to 45 m. It shows the grid search results for main FZ parameters based on waveform inversion. The optimal FZ model parameters are as follows: the center of FZ is located 25 m to the northeast of

the surface fault trace, the FZ depth is 165 m, the half-width of the fault zone is 35 m, so the total width is 35*2 = 70 m, the dip angle relative to the Z-direction is 35°, and the Vp reduction is 45% of the host rock velocity. The misfit matrix of the dip angle and central location (horizontal shift value relative to the surface fault trace) of the FZ at the optimal values of velocity reduction ratio, width and depth. There is trade-off between the dip angle and the FZ central location, but this does not affect the determination of the optimal dip angle and FZ central location.

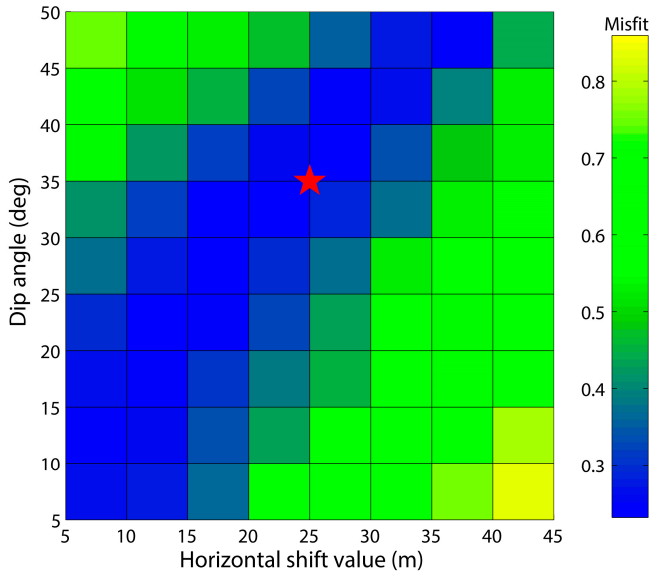

Figure 10. The misfit 2D maps of the dip angle and central location (horizontal shift value relative to the surface fault trace) of the FZ at the optimal values of velocity reduction ratio, width and depth. Trade-off between the dip angle and the fault zone central location can be observed.

4.5. Inversion Algorithm

In the previous section of the study, we preliminarily determined that the fault dip was 35~40° and the fault core was located 20~25 m. In this section, we will adjust the width and depth of the fault model to the greatest extent possible using the P-wave to fit the observed travel time curves. The fault parameters are listed in Table 1, and after searching through ~86,000 models using a grid-based approach, we selected several models with better travel time curve fitting. As shown in Figure 11, the depth of the fault zone is 165 m and the width is ~70 m. We also considered the factors of P-wave travel time and incoming angle, and fitted them to improve effect of the model, so as to maximize the NCC value.

The results reflect the high resolution in the seismic inversion process based on the P-wave travel time. In Figures A3–A6, we show the sensitivity of each model parameter, through observing the change in the travel time curve by slightly adjusting different parameters. Among them, the travel time curve is the most sensitive to the parameter of the FZ core location, and adjusting the location of the FZ core will greatly affect the NCC value. Finally, we compared the theoretical P-wave incoming angles of the optimal models with the actual observed incoming angles (Figure 11). Moreover, the fitting effect was relatively good.

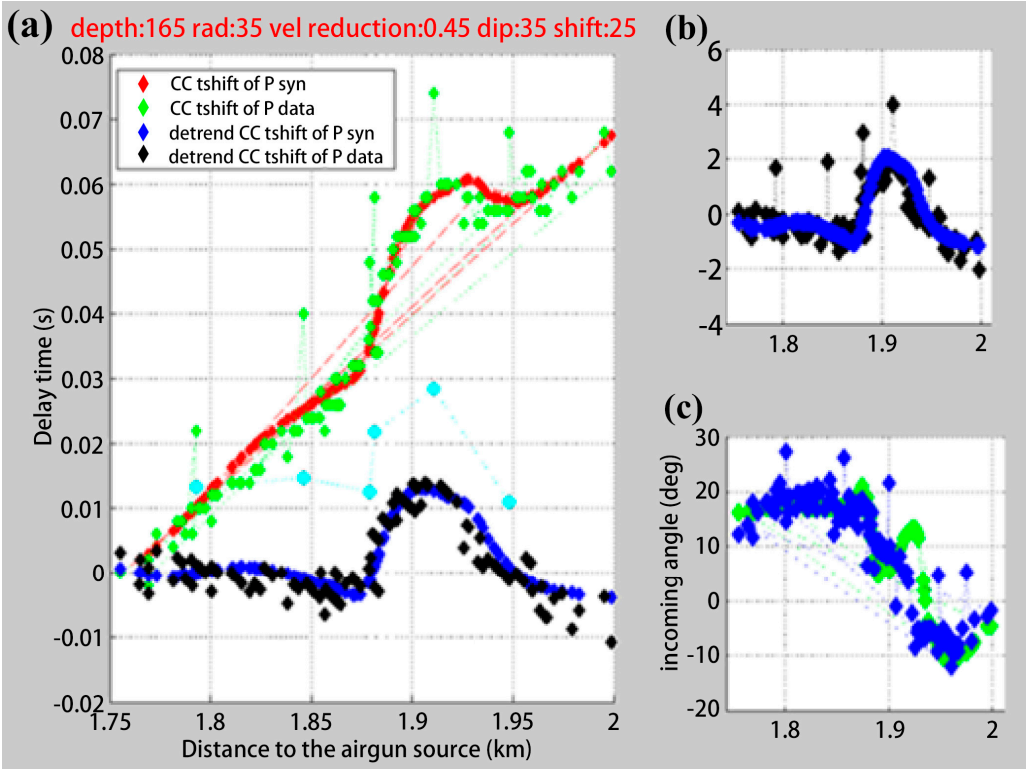

Figure 11. (**a**) P-wave arrival times curve of observations (green) and predictions (red) near the FZ and their modification value after detrending. (**b**) Delay time curve of observation and prediction after detrending and equal scaling in (**a**). (**c**) Observed P-wave incoming angle (blue dots) and P-wave incoming angle (green dots) of fault zone velocity model in (**a**).

5. Discussion

In this study, we investigated the Xiliushui fault zone structure by modeling the P-wave travel times of the airgun source recorded by a temporary linear ultra-dense array and multiple observations. Using the spectral element method, we found a 70–80 m-wide inactive FZ and the P-wave velocity reduction in the FZ was about 45%, like other typical inactive faults' velocity reduction [64]. Based on a systematic analysis of travel times from both sides of the fault, we found the FZ is not vertical but dips about 30–40° southwest. In addition, the FZ extends to 100–125 m in depth. The different FZ dip may lead to a trade-off in estimating the depth and width of the fault, which may reflect the non-uniqueness of the solution in the seismic inversion. Up to now, constraining the depth and extent of the fault has been challenging. Unlike other typical faults, the fault depth obtained by the waveform travel time inversion is very shallow, which is related to the limited observation data. Considering the lack of large earthquakes along the Xiliushui fault, the fault core zone must have persisted for thousands of years or longer. Even though the best-fit solution is not unique and the model parameters trade off each other, a study of parameter sensitivity, comparing synthetics with recorded data, indicates that the variability in the depth and velocity reduction can be restricted to a limited range of value.

The FZ's width in the Xiliushui fault is narrower than other typical faults, while the Hector Mine FZ's width is 70–100 m, the Landers FZ's width is about 200 m [65,66], and the width of the Kunlun mountain FZ is about 300 m [67], among the other crustal faults studied using seismic waves. By investigating the development of rupture distributions as a function of displacement, Savage [68] suggested that the width of the fault damage zone is proportional to the total displacement accumulated along the fault. Therefore, we infer that the Xiliushui fault has yet to experience significant displacement accumulation. The

narrow fault width and depth may have also resulted from long-term fault healing, which needs further study.

The Rayleigh waves and their code wave were also observed by the airgun seismic source, which has the characteristics of a large amplitude and low frequency compared with the P-wave and Rayleigh wave. This trapped wave property is produced within the fault zone and is more sensitive to the width of the fault zone, which is helpful for us to better understand the width of the fault zone.

Under the inactive fault test in the research area, due to the lack of local events and the frequency of teleseismic waves being too low to improve the imaging solution, it is necessary to consider using the ambient seismic noise to image shallow S-wave velocity and the instrument deployment time needs to be longer. In addition, we can verify our understanding of the fine structure of the Xiliushui fault zone by studying the properties of resonance waves in future research [16].

6. Conclusions

In this study, we used an artificial airgun source with high repeatability and environmental protection on the inactive old Xiliushui fault zone in the northeastern margin of the Tibetan Plateau, China. We carefully picked high-frequency P-body wave travel time curves in the 5–20 Hz frequency band. According to the considerable velocity delay variation in the fault zone, we used a direct 2D spectral element method (SEM) to fit the P-wave travel time delay curve, considering the topography and host rock with a linear velocity gradient. The inversion results show a fault zone structure with a width of 70–80 m, depth of ~165 m, dip of 30–35°, and velocity reduction of ~45% compared to the host rock.

This study can help us better understand the complex fault structures in this area with a high repeatability and environmental-friendly method. As a new method based on an ultra-dense array, it provides a new perspective for future research on the velocity structure of shallow fault zones with high resolution.

Author Contributions: Conceptualization, M.Q. and B.W.; methodology, Y.W. (Yi Wang) and B.W.; software, Y.W. (Yi Wang) and B.W.; validation, Y.W. (Yi Wang) and B.W.; formal analysis, Y.W. (Yi Wang) and B.W.; investigation, D.S. and Y.W. (Yahong Wang); resources, R.Z., X.L. and X.G.; data curation, M.Q.; writing—original draft preparation, B.W.; writing—review and editing, B.W. and Y.W. (Yi Wang); visualization, B.W.; supervision, Y.W. (Yi Wang); project administration, X.S.; funding acquisition, Y.Z. All authors have read and agreed to the published version of the manuscript.

Funding: This research is supported by the Basic Research Fund of the Institute of Earthquake forecasting, China Earthquake Administration (CEAIEF20220203, CEAIEF2024030102), and Science for Earthquake Resilience, China Earthquake Administration (XH20060).

Data Availability Statement: The waveform data of the airgun seismic sources and crust model used in this study are available at https://doi.org/10.5061/dryad.8931zcrzt.

Acknowledgments: The figures in this study were produced using the Generic Mapping Tools (GMT) software package (version 6.2) and ObsPy software package (version 1.0, based on Python). All the synthetic models were constructed and imaged using SPECFEM2D (version 8.1).

Conflicts of Interest: The authors declare no conflict of interest.

Appendix A

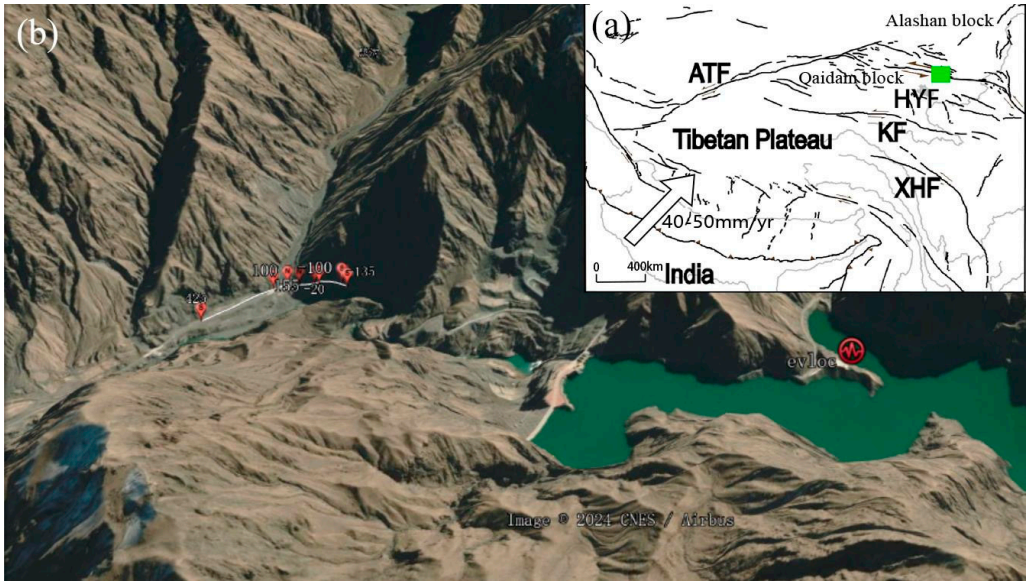

Figure A1. The location of the Gansu Qilian Mountain active seismic source (**a**), and the aerial view of reservoir and topography in the study area. (**a**) Regional geotectonic map; the green rectangle is the research area in Figure 1. HYF is Qilian-Haiyuan Fault; ATF is Altyn-Tagh Fault; KF is Kunlun Fault; XHF is Xianshuihe Fault. (**b**) The red circle represents airgun source, the red points represent stations in the array (white line).

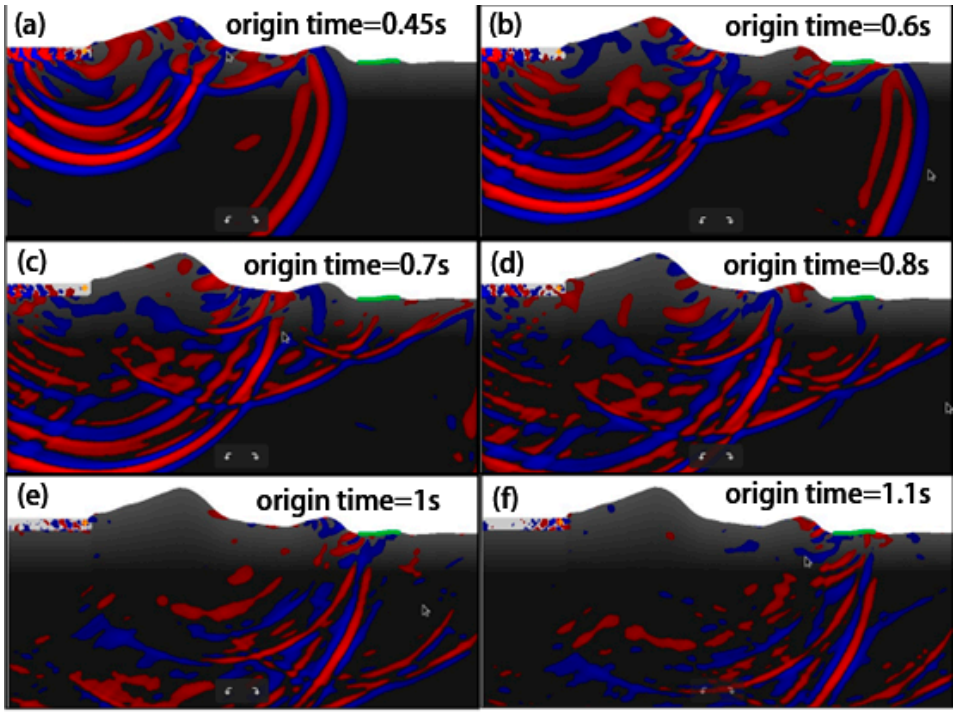

Figure A2. Flash snapshot in basic forward model. The red and blue represent wavefield; green represents array zone. (**a**–**f**) is the wave field snapshot at different source times.

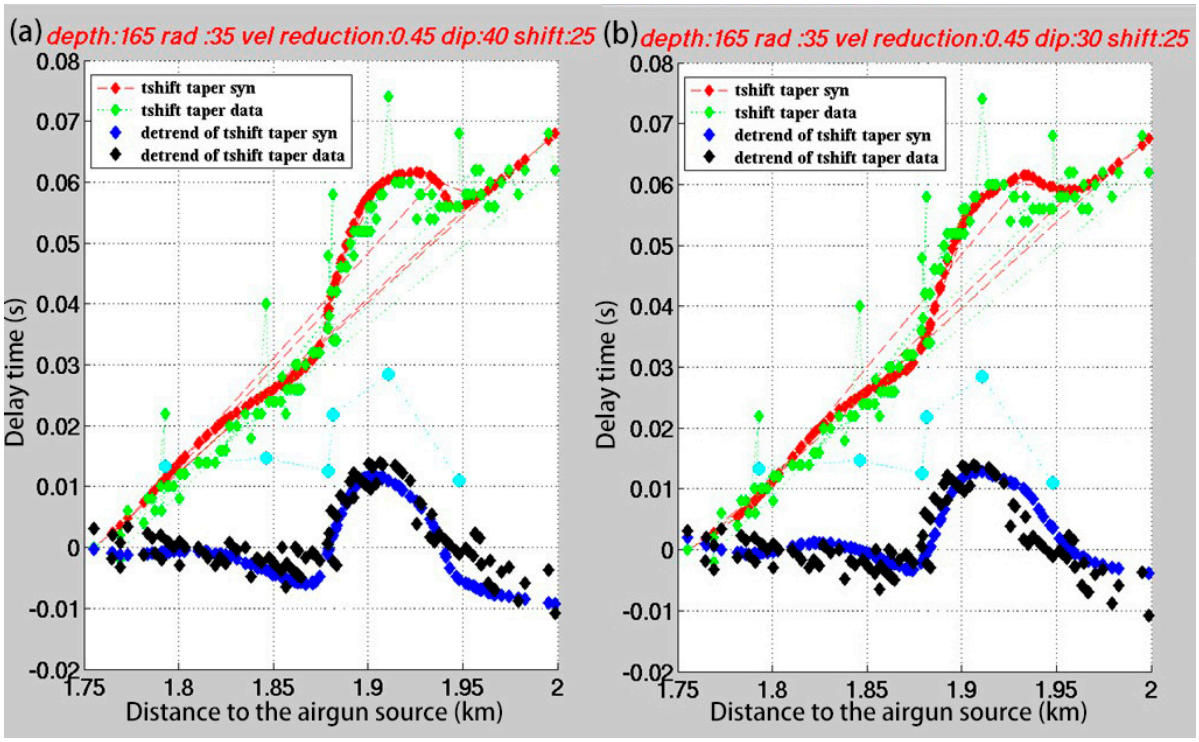

Figure A3. P-wave arrival times curve and predictions of different models near the FZ. Adjusting dip of FZ (±5°) based on optimal FZ's parameter model. (**a**) dip: 35° + 5°, detrend NCC value of travel delay time is 0.8; (**b**) dip: 35° − 5°, detrend NCC value of travel delay time is 0.73.

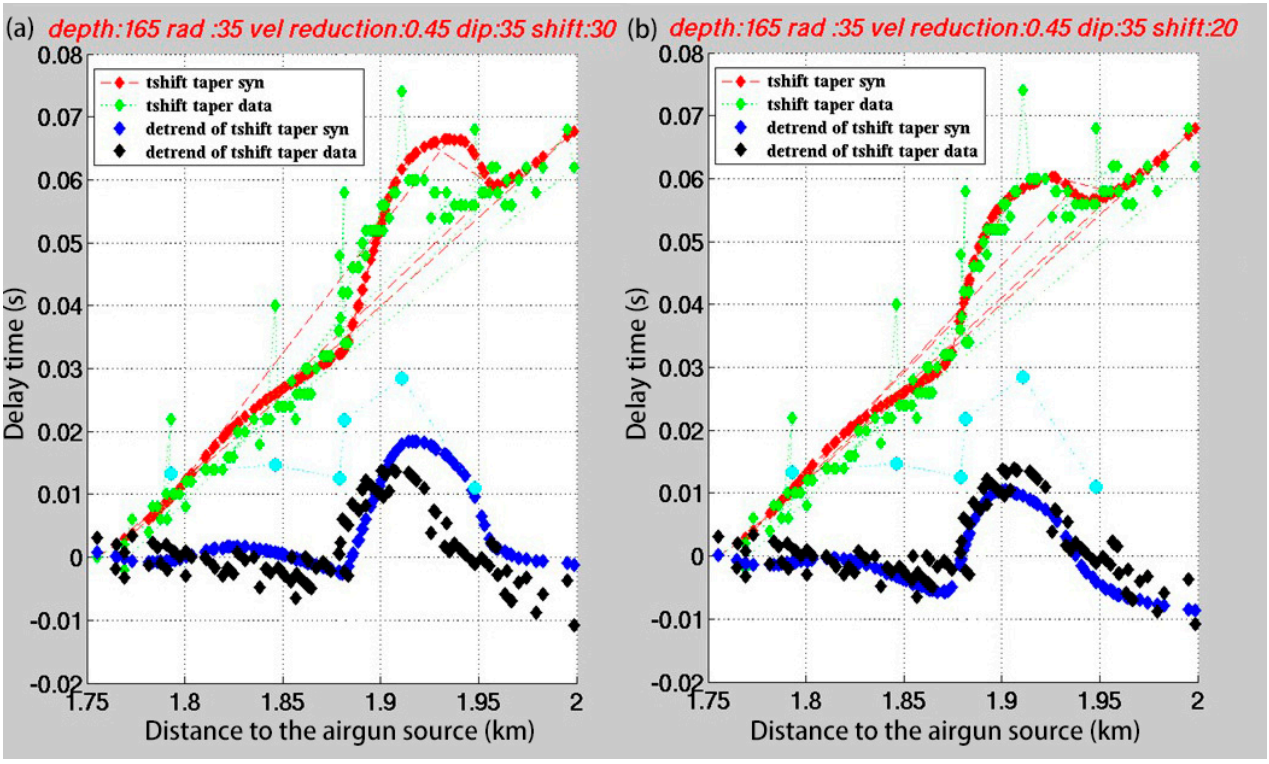

Figure A4. P-wave arrival times curve and predictions of different models near the FZ. Adjusting location of FZ core (±5 m) based on optimal FZ's parameter model. (**a**) FZ core location: 25 m + 5 m, detrend NCC value of travel delay time is 0.58; (**b**) dip: 25 m − 5 m, detrend NCC value of travel delay time is 0.8.

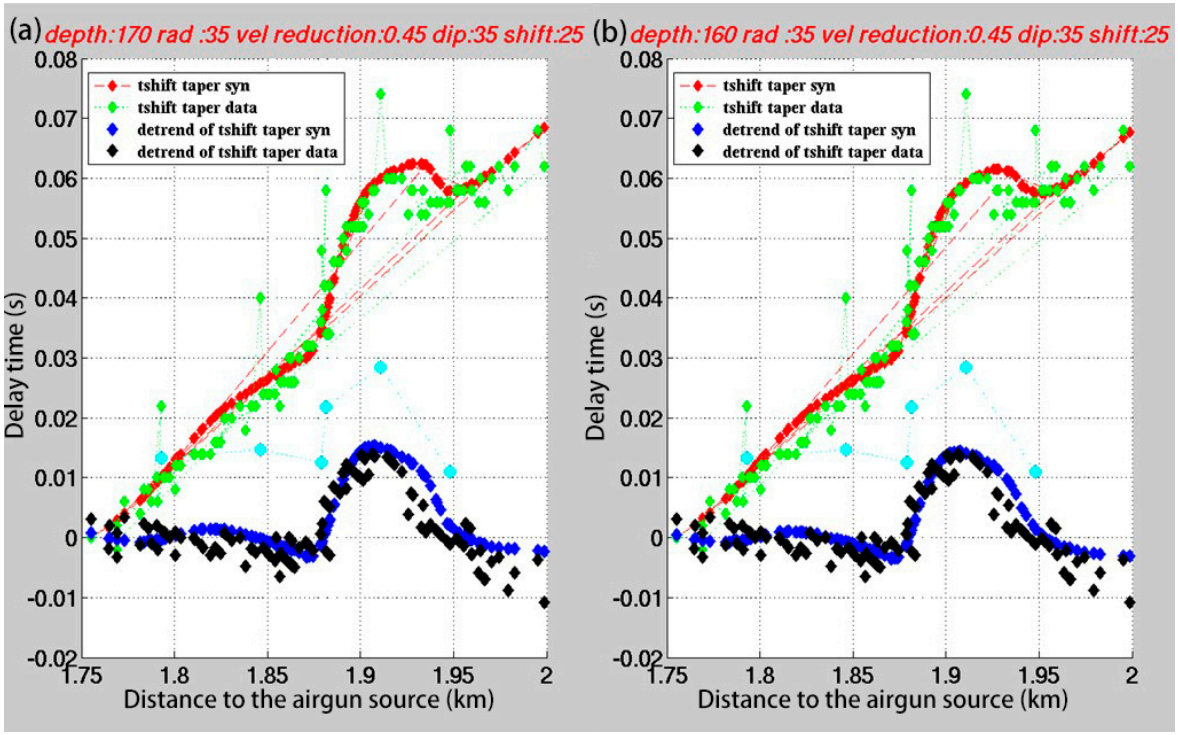

Figure A5. P-wave arrival times curve and predictions of different models near the FZ. Adjusting depth of FZ (±5 m) based on optimal FZ's parameter model. (**a**) FZ's depth: 165 m + 5 m, detrend NCC value of travel delay time is 0.76; (**b**) FZ's depth: 165 m− 5 m, detrend NCC value of travel delay time is 0.77.

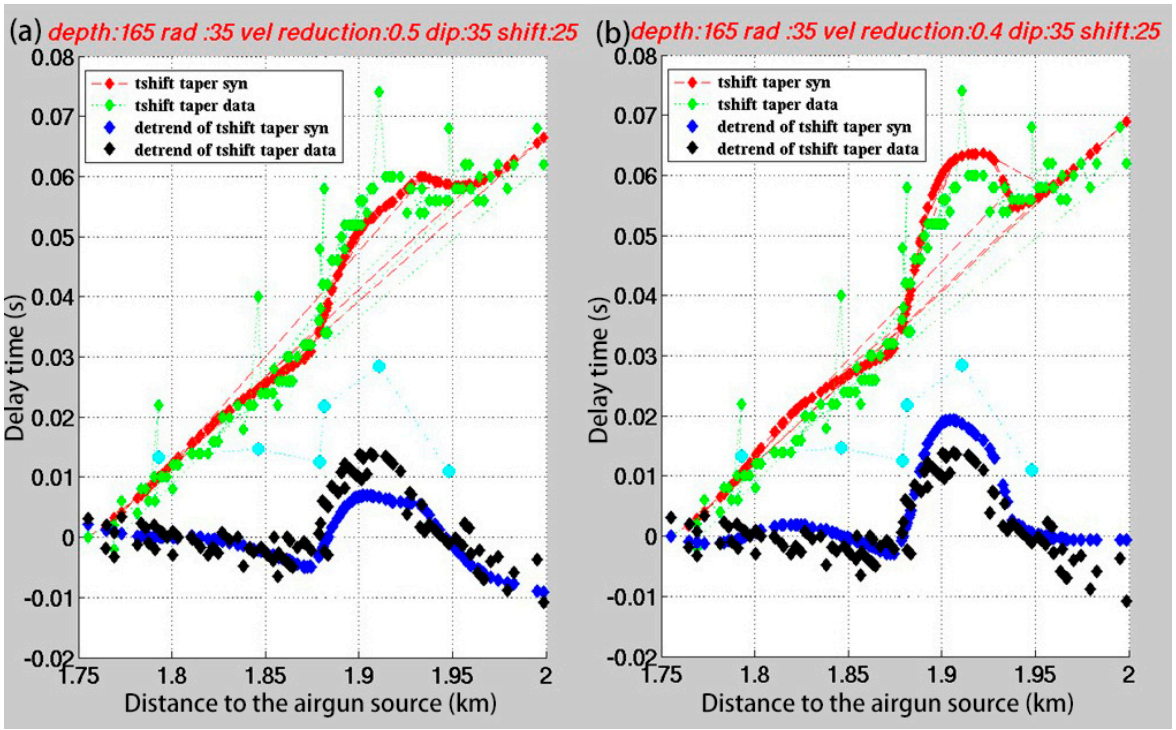

Figure A6. P-wave arrival times curve and predictions of different models near the FZ. Adjusting velocity reduction of FZ (45%) based on optimal FZ parameter model. (**a**) FZ velocity reduction to 45% + 5%; detrend in NCC value of travel delay time is 0.75; (**b**) FZ velocity reduction to 45% − 5%; detrend in NCC value of travel delay time is 0.77.

References

1. Chen, Y.; Wang, B.; Yao, H. Seismic Airgun Exploration of Continental Crust Structures. *Sci. China Earth Sci.* **2017**, *60*, 1739–1751. [CrossRef]
2. Mallet, R. *Second Report on the Facts of Earthquake Phaenomena*; Taylor & Francis: Boca Raton, FL, USA, 1852.
3. Mueller, S.; Peterschmitt, E.; Fuchs, K.; Ansorge, J. Crustal Structure beneath the Rhinegraben from Seismic Refraction and Reflection Measurements. *Tectonophysics* **1969**, *8*, 529–542. [CrossRef]
4. Zelt, C.A.; Ellis, R.M.; Zelt, B.C. Three-dimensional structure across the Tintina strike-slip fault, northern Canadian Cordillera, from seismic refraction and reflection tomography. *Geophys. J. Int.* **2006**, *167*, 1292–1308. [CrossRef]
5. Prodehl, C.; Mooney, W.D. *Exploring the Earth's Crust: History and Results of Controlled-Source Seismology*; Geological Society of America: Boulder, CO, USA, 2012.
6. Chen, Y.; Zhang, X.K.; Qiu, X.L.; Ge, H.K.; Liu, J.B.; Wang, B.S. A new method for the artificial excitation of earthquake waves on land. *Chin. Sci. Bull.* **2007**, 1–5. (In Chinese)
7. Wang, B.S.; Wang, W.T.; Ge, H.K.; Xu, P.; Wang, B. Monitoring subsurface changes with active sources. *Adv. Earth Sci.* **2011**, *26*, 249–256. (In Chinese)
8. Qiu, X.; Chen, Y.; Zhu, R.; Xu, H.; Shi, X.; Ye, C.; Zhao, M.; Xia, S. The application of large volume airgun sources to the onshore-offshore seismic surveys: Implication of the experimental results in northern South China Sea. *Chin. Sci. Bull.* **2007**, *52*, 553–560. [CrossRef]
9. Zhou, B.H.; Liu, W.B. The development and application of air-gun source (1). *Equip. Geophys. Prosp.* **1998**, *8*, 1–6. (In Chinese)
10. Reasenberg, P.; Aki, K. A precise continuous measurement of seismic velocity for monitoring in situ stress. *J Geophys Res.* **1974**, *79*, 399–406. [CrossRef]
11. Chen, Y.; Wang BSh Ge, H.K.; Xu, P.; Zhang, W. Proposed of transmitted seismic stations. *Adv. Earth Sci.* **2007**, *22*, 441–446. (In Chinese)
12. Chen, Y.; Liu, L.; Ge, H.; Liu, B.; Qiu, X. Using an airgun array in a land reservoir as the seismic source for seismotectonic studies in northern China: Experiments and preliminary results. *Geophys. Prospect.* **2008**, *56*, 601–612. [CrossRef]
13. Yang, W.; Wang, B.S.; Ge, H.K.; Wang, W.T.; Chen, Y. The active monitoring system with large volume airgun seismic source and experiment. *Earthq. Res. China* **2013**, *29*, 399–410. (In Chinese)
14. Qiu, H.; Ben-Zion, Y.; Catchings, R.; Goldman, M.R.; Allam, A.A.; Steidl, J. Seismic imaging of the Mw 7.1 Ridgecrest earthquake rupture zone from data recorded by dense linear arrays. *J. Geophys. Res. Solid Earth* **2021**, *126*, e2021JB022043. [CrossRef]
15. Yang, H.; Duan, Y.; Song, J.; Jiang, X.; Tian, X.; Yang, W.; Wang, W.; Yang, J. Fine Structure of the Chenghai Fault Zone, Yunnan, China, Constrained from Teleseismic Travel Time and Ambient Noise Tomography. *J. Geophys. Res. Solid Earth* **2020**, *125*, e2020JB019565. [CrossRef]
16. McGuire, J.J.; Boettcher, M.S.; Jordan, T.H. Foreshock Sequences and Short-Term Earthquake Predictability on East Pacific Rise Transform Faults. *Nature* **2005**, *434*, 457–461. [CrossRef] [PubMed]
17. Qin, L.; Ben-Zion, Y.; Qiu, H.; Share, P.-E.; Ross, Z.E.; Vernon, F.L. Internal Structure of the San Jacinto Fault Zone in the Trifurcation Area Southeast of Anza, California, from Data of Dense Seismic Arrays. *Geophys. J. Int.* **2018**, *213*, 98–114. [CrossRef]
18. Yang, H.; Zhu, L. Shallow Low-Velocity Zone of the San Jacinto Fault from Local Earthquake Waveform Modelling: San Jacinto Fault Structure from Body Waves. *Geophys. J. Int.* **2010**, *183*, 421–432. [CrossRef]
19. Lewis, M.A.; Peng, Z.; Ben-Zion, Y.; Vernon, F.L. Shallow Seismic Trapping Structure in the San Jacinto Fault Zone near Anza, California. *Geophys. J. Int.* **2005**, *162*, 867–881. [CrossRef]
20. Jiang, X.; Hu, S.; Yang, H. Depth Extent and Vp/Vs Ratio of the Chenghai Fault Zone, Yunnan, China Constrained from Dense-Array-Based Teleseismic Receiver Functions. *J. Geophys. Res. Solid Earth* **2021**, *126*, e2021JB022190. [CrossRef]
21. Zhang, Y.S.; Guo, X.; Qin, M.Z.; Liu, X.Z.; Wei, C.X.; Shen, X.Z.; Yan, W.H.; Zou, R.; Yin, L.; Wang, Y.H. The construction of active source repeated monitoring in the Qilan Mountains of Gansu Province. *Earthq. Res. China* **2016**, *2*, 209–215. (In Chinese)
22. Qin, M.Z.; Liu, X.Z.; Zou, R.; Zhang, Y.S.; Guo, X.; Wei, C.X.; Wang, Y.H.; Sun, D.F. Maximum detective range of the large-volume airgun active source in Qilian Mountains, Gansu Province. *China Earthq. Eng. J.* **2017**, *39*, 1070–1075. (In Chinese)
23. Wei, C.; Qin, M.; Zhang, Y.; Zou, R.; Wang, L.; Guo, X.; Liu, X.; Wang, Y.; Sun, D. Airgun Excitation Experiments at Different Placement Depths in the Qilian Mountain of Gansu Province, China. *Seismol. Res. Lett.* **2018**, *89*, 974–982. [CrossRef]
24. Wang, B.; Tian, X.; Zhang, Y.; Li, Y.; Yang, W.; Zhang, B.; Wang, W.; Yang, J.; Li, X. Seismic Signature of an Untuned Large-volume Airgun Array Fired in a Water Reservoir. *Seismol. Res. Lett.* **2018**, *89*, 983–991. [CrossRef]
25. Li, Y.L.; Xing, C.Q. Research on the fundamental characteristics of the geological structures of the Hexi Corridor and the active faults of the northern and eastern flank of the Yumushan Mountain. *Northwestern Seismol. J.* **1988**, *10*, 35–47.
26. Chu, Q.Z.; Wang, L.M.; Guo, S.M. Segmentation and risk estimation of earthquake on Qilianshan active fault zone. *Seismol. Geol.* **1995**, *29*, 399–410. (In Chinese)
27. Zhu, Z.Z.; Yao, J.L. Study on the seismicity features of Mt. Qilian seismic zone. *Northwestern Seismol. J.* **1997**, *19*, 25–30. (In Chinese)

28. Li, Y.-G.; Vidale, J.E.; Aki, K.; Xu, F. Depth-dependent Structure of the Landers Fault Zone from Trapped Waves Generated by Aftershocks. *J. Geophys. Res.* **2000**, *105*, 6237–6254. [CrossRef]
29. Ronen, S. Psi, pascal, bars, and decibels. *Lead. Edge.* **2002**, *21*, 60–61. [CrossRef]
30. Wang, B.; Wu, G.H.; Su, Y.J.; Wang, B.S.; Ge, H.K.; Jin, M.P.; Yang, J.; Zhang, Q.M.; Li, T.; Liu, J.W. Site selection and construction process of Binchuan earthquake signal transmitting seismic station and its preliminary observation result. *J. Seismol. Res.* **2015**, *38*, 1–6.
31. Zhao, M.-H.; Qiu, X.-L.; Wang, P.; Xia, S.-H.; Li, Y.-M.; Xu, H.-L.; Ye, C.-M.; Kang, Y. Large Volume Air-gun Sources and Its Seismic Waveform Characters. *Chin. J. Geophys.* **2008**, *51*, 400–408. [CrossRef]
32. Li, Y.; Malin, P.; Cochran, E.S.; Chen, P. High-Resolution Imaging of the San Andreas Fault Damage Zone from SAFOD Main-Hole and Surface Seismic Records. *InAGU Fall Meet. Abstr.* **2010**, *2010*, T41A-2085.
33. Song, J.; Yang, H. Seismic Site Response Inferred from Records at a Dense Linear Array across the Chenghai Fault Zone, Binchuan, Yunnan. *J. Geophys. Res. Solid Earth* **2022**, *127*, e2021JB022710. [CrossRef]
34. Borcherdt, R.D. Effects of local geology on ground motion near San Francisco Bay. *Bull. Seismol. Soc. Am.* **1970**, *60*, 29–61.
35. Zhou, G.; Yao, H. Shallow Structure and Seismic Amplification Effects in the Weifang Segment of the Tanlu Fault Zone Based on the Spectral Ratio Method. *Seismol. Res. Lett.* **2025**, *96*, 435–448. [CrossRef]
36. Pratt, T.L.; Horton, J.W., Jr.; Muñoz, J.; Hough, S.E.; Chapman, M.C.; Olgun, C.G. Amplification of earthquake ground motions in Washington, DC, and implications for hazard assessments in central and eastern North America. *Geophys. Res. Lett.* **2017**, *44*, 12–50. [CrossRef]
37. Ma, X.; Wang, W.; Xu, S.; Yang, W.; Zhang, Y.; Dong, C. Imaging the Fault Zone Structure of the Pearl River Estuary Fault in Guangzhou, China, from Waveform Inversion with an Active Source and Dense Linear Array. *Remote Sens.* **2023**, *15*, 254. [CrossRef]
38. Zhao, L.; Jordan, T.H.; Chapman, C.H. Three-Dimensional Frechet Differential Kernels for Seismicdelay Times. *Geophys. J. Int.* **2000**, *141*, 558–576. [CrossRef]
39. Virieux, J.; Operto, S. An Overview of Full-Waveform Inversion in Exploration Geophysics. *Geophysics* **2009**, *74*, WCC1–WCC26. [CrossRef]
40. Li, H.; Gao, R.; Li, W.; Carbonell, R.; Yelisetti, S.; Huang, X.; Shi, Z.; Lu, Z. The Mabja Dome Structure in Southern Tibet Revealed by Deep Seismic Reflection Data and Its Tectonic Implications. *J. Geophys. Res. Solid Earth* **2021**, *126*, e2020JB020265. [CrossRef]
41. Li, X.; Yao, G.; Niu, F.; Wu, D.; Liu, N. Waveform Inversion of Seismic First Arrivals Acquired on Irregular Surface. *Geophysics* **2022**, *87*, R291–R304. [CrossRef]
42. Borisov, D.; Gao, F.; Williamson, P.; Tromp, J. Application of 2D Full-Waveform Inversion on Exploration Land Data. *Geophysics* **2020**, *85*, R75–R86. [CrossRef]
43. Sheng, J.; Leeds, A.; Buddensiek, M.; Schuster, G.T. Early Arrival Waveform Tomography on Near-Surface Refraction Data. *Geophysics* **2006**, *71*, U47–U57. [CrossRef]
44. Warner, M.; Guasch, L. Adaptive waveform inversion-FWI without cycle skipping-theory. In Proceedings of the 76th EAGE Conference and Exhibition 2014, Amsterdam, The Netherlands, 16–19 June 2014; Volume 2014, pp. 1–5.
45. Wu, R.-S.; Luo, J.; Wu, B. Seismic Envelope Inversion and Modulation Signal Model. *Geophysics* **2014**, *79*, WA13–WA24. [CrossRef]
46. Luo, Y.; Schuster, G.T. Wave-equation traveltime inversion. *Geophysics* **1991**, *56*, 645–653. [CrossRef]
47. Moczo, P.; Kristek, J.; Galis, M.; Pazak, P.; Balazovjech, M. The finite-difference and finite-element modeling of seismic wave propagation and earthquake motion. *Acta Phys. Slovaca* **2007**, *57*, 177–406. [CrossRef]
48. Fichtner, A. *Full Seismic Waveform Modelling and Inversion*; Springer Science & Business Media: Berlin/Heidelberg, Germany, 2010.
49. Furumura, T.; Kennett, B.L.; Furumura, M. Seismic wavefield calculation for laterally heterogeneous whole earth models using the pseudospectral method. *Geophys. J. Int.* **1998**, *135*, 845–860. [CrossRef]
50. Zhan, W.; Zhuang, M.; Liu, Q.Q.; Shi, L.; Sun, Y.; Liu, Q.H. Frequency Domain Spectral Element Method for Modelling Poroelastic Waves in 3-D Anisotropic, Heterogeneous and Attenuative Porous Media. *Geophys. J. Int.* **2021**, *227*, 1339–1353. [CrossRef]
51. Faccioli, E.; Maggio, F.; Paolucci, R.; Quarteroni, A. 2D and 3D elastic wave propagation by a pseudo-spectral domain decomposition method. *J. Seismol.* **1997**, *1*, 237–251. [CrossRef]
52. Tromp, J.; Komatitsch, D.; Liu, Q. Spectral-element and adjoint methods in seismology. *Commun. Comput. Phys.* **2008**, *3*, 1–32.
53. Gholamy, A.; Kreinovich, V. Why Ricker Wavelets Are Successful in Processing Seismic Data: Towards a Theoretical Explanation. In Proceedings of the 2014 IEEE Symposium on Computational Intelligence for Engineering Solutions (CIES), Orlando, FL, USA, 9–12 December 2014.
54. Graves, R.W. Simulating seismic wave propagation in 3D elastic media using staggered-grid finite differences. *Bull. Seismol. Soc. Am.* **1996**, *86*, 1091–1106. [CrossRef]
55. Robertsson, J.O. A numerical free-surface condition for elastic/viscoelastic finite-difference modeling in the presence of topography. *Geophysics* **1996**, *61*, 1921–1934. [CrossRef]

56. Komatitsch, D.; Tromp, J. Introduction to the spectral element method for three-dimensional seismic wave propagation. *Geophys. J. Int.* **1999**, *139*, 806–822. [CrossRef]
57. Sengbush, R.L. Theory of seismic wave propagation. In *Petroleum Exploration: A Quantitative Introduction*; Springer: Dordrecht, The Netherlands, 1986; Volume 771, pp. 127–147.
58. Hess, P. Surface acoustic waves in materials science. *Physics Today* **2002**, *55*, 42–47. [CrossRef]
59. Withjack, M.O.; Pollock, D.D. Synthetic seismic-reflection profiles of rift-related structures. *AAPG Bull.* **1984**, *68*, 1160–1178.
60. Fagin, S.W. *Seismic Modeling of Geologic Structures: Applications to Exploration Problems*; Society of Exploration Geophysicists: Houston, TX, USA, 1991.
61. Morse, P.F.; Purnell, G.W.; Medwedeff, D.A. 9. Case History 4 Seismic Modeling of Fault-Related Folds. In *Seismic Modeling of Geologic Structures*; Society of Exploration Geophysicists: Houston, TX, USA, 1991; pp. 127–152.
62. Alaei, B.; Petersen, S.A. Geological Modelling and Finite Difference Forward Realization of a Regional Section from the Zagros Fold-and-Thrust Belt. *Pet. Geosci.* **2007**, *13*, 241–251. [CrossRef]
63. Li, J.; Mitra, S. Seismic Modeling and Expression of Common Fold-Thrust Structures. *Interpretation* **2020**, *8*, T55–T65. [CrossRef]
64. Rovelli, A. Can Seismic Waves Be Trapped inside an Inactive Fault Zone? The Case Study of Nocera Umbra, Central Italy. *Bull. Seismol. Soc. Am.* **2002**, *92*, 2217–2232. [CrossRef]
65. Li, Y.G.; Aki, K.; Vidale, J.E.; Lee, W.H.; Marone, C.J. Fine Structure of the Landers Fault Zone: Segmentation and the Rupture Process. *Science* **1994**, *265*, 367–370. [CrossRef]
66. Li, Y.G.; Vidale, J.E.; Day, S.M.; Oglesby, D.D. Study of the 1999 M 7.1 Hector Mine, California, earthquake fault plane by trapped waves. *Bull. Seismol. Soc. Am.* **2002**, *92*, 1318–1332. [CrossRef]
67. Li, S.L.; Zhang, X.K.; Fan, J.C. Study on rupture zone of the M = 8.1 Kunlun mountain earthquake using fault-zone trapped waves. *Acta Seismol. Sin.* **2005**, *27*, 42–50. (In Chinese) [CrossRef]
68. Savage, H.M.; Brodsky, E.E. Collateral damage: Evolution with displacement of fracture distribution and secondary fault strands in fault damage zones. *J. Geophys. Res. Solid Earth* **2011**, *116*. [CrossRef]